

# The Merger Fraction of Ultramassive White Dwarfs

Mukremin Kilic<sup>1</sup>, Adam G. Moss<sup>1</sup>, Alekzander Kosakowski<sup>2</sup>, P. Bergeron<sup>3</sup>,  
Annamarie A. Conly<sup>4</sup>, Warren R. Brown<sup>5</sup>, Silvia Toonen<sup>6</sup>, Kurtis A. Williams<sup>7</sup>, P. Dufour<sup>3</sup>

<sup>1</sup>Homer L. Dodge Department of Physics and Astronomy, University of Oklahoma, 440 W. Brooks St., Norman, OK 73019, USA

<sup>2</sup>Department of Physics and Astronomy, Texas Tech University, Lubbock, TX 79409, USA

<sup>3</sup>Département de Physique, Université de Montréal, C.P. 6128, Succ. Centre-Ville, Montréal, QC H3C 3J7, Canada

<sup>4</sup>Department of Astronomy, New Mexico State University, Las Cruces, NM 88003, USA

<sup>5</sup>Smithsonian Astrophysical Observatory, 60 Garden Street, Cambridge, MA 02138, USA

<sup>6</sup>Anton Pannekoek Institute for Astronomy, University of Amsterdam, 1090 GE Amsterdam, The Netherlands

<sup>7</sup>Department of Physics & Astronomy, Texas A&M University-Commerce, Commerce, TX 75429, USA

Submitted 14 November 2022

## ABSTRACT

We search for merger products among the 25 most massive white dwarfs in the Montreal White Dwarf Database 100 pc sample through follow-up spectroscopy and high-cadence photometry. We find an unusually high fraction, 40%, of magnetic white dwarfs among this population. In addition, we identify four outliers in transverse velocity and detect rapid rotation in five objects. Our results show that  $56^{+9}_{-10}$ % of the  $M \approx 1.3 M_{\odot}$  ultramassive white dwarfs form through mergers. This fraction is significantly higher than expected from the default binary population synthesis calculations using the  $\alpha$ -prescription (with  $\alpha\lambda = 2$ ), and provides further support for efficient orbital shrinkage, such as with low values of the common envelope efficiency.

**Key words:** stars: evolution — stars: magnetic field — stars: rotation — white dwarfs

## 1 INTRODUCTION

Binary stars are common, but binary white dwarfs are less so. The multiplicity fraction of A type stars, the dominant progenitor systems for white dwarfs in the solar neighborhood, is around 45% (De Rosa et al. 2014; Moe & Di Stefano 2017), whereas that of the white dwarfs in the local 20–25 pc sample is significantly lower at  $\approx 25\%$  (Holberg et al. 2016; Hollands et al. 2018). This discrepancy is not simply due to observational biases against detecting a dim white dwarf companion close to a bright star, but instead it can be explained if a significant fraction of the binary systems disappear on or after the main-sequence phase through mergers, and form single stars that evolve into single white dwarfs (Toonen et al. 2017; Temmink et al. 2020).

Accreting CO core white dwarfs as well as mergers of double white dwarfs can reach the Chandrasekhar limit and explode as type Ia supernovae (Webbink 1984; Iben & Tutukov 1984). Sub-Chandrasekhar-mass white dwarfs can also detonate (e.g. Shen et al. 2018). However, due to the steepness of the initial mass function, most merger events involve lower mass white dwarfs, and they do not lead to explosive transient events. Instead they form single, more massive white dwarfs (García-Berro et al. 2012; Schwab 2021). Based on binary population synthesis calculations, Temmink et al. (2020) estimated that between about 10 to 30% of all single white dwarfs are formed through binary mergers, with the majority of them involving the descendants of mergers between post-main-sequence and main-sequence stars. However, the predicted merger fraction goes up to 30 to 45% for all observable single white dwarfs with  $M > 0.9 M_{\odot}$  and within 100 pc of the Sun.

Observational constraints on the merger fraction of single white

dwarfs are scarce. Maoz et al. (2012), Maoz & Hallakoun (2017), and Maoz et al. (2018) used a statistical method for characterizing the binary white dwarf population in the Sloan Digital Sky Survey and the ESO-VLT Supernova-Ia to estimate that 8.5 to 11% of all white dwarfs ever formed have merged with another white dwarf. This is significantly higher than predicted from the binary population synthesis models,  $\sim 1$ –3%, of Temmink et al. (2020), and if true, has implications for the type Ia supernova progenitors (Maoz et al. 2018; Cheng et al. 2020) and the gravitational wave foreground from the Galactic double white dwarf population in the milli-Hertz frequency band (Korol et al. 2022).

Kilic et al. (2021a) presented an analysis of the 25 most massive ( $M \geq 1.3 M_{\odot}$ ) white dwarf candidates in the Montreal White Dwarf Database 100 pc sample and concluded that at least 32% of these white dwarfs are likely double white dwarf merger products based on their kinematics, magnetism, or rapid rotation. However, only 10 of these objects currently have spectral classification available, and interestingly, four are magnetic. Tout et al. (2008) and Briggs et al. (2015) argued that all strongly magnetic white dwarfs have a binary origin, as a magnetic dynamo can be generated during a merger event though differential rotation within a common-envelope or an accretion disk. In addition, only one of these targets, J1832+0856, had follow-up high cadence photometry available, which revealed a spin period of only 353 s (Pshirkov et al. 2020). The fraction of merger products among the ultramassive white dwarfs may be much higher.

Recently, Caiazzo et al. (2021) found a rotation period of 6.94 min in another object in this sample, J1901+1458, and Kilic et al. (2021b) discovered photometric variations in J2211+1136 with a

period of only 70 s, making it the fastest spinning isolated white dwarf currently known. These rotation rates are consistent with the predicted rates for single white dwarfs that formed from double white dwarf mergers (Schwab 2021).

Here we present the results from a spectroscopic and photometric follow-up survey of all 25 ultramassive white dwarfs identified by Kilic et al. (2021a). We use the optical spectroscopy of the remaining targets to search for evidence of magnetism and unusual atmospheric composition that would indicate a merger origin, and high-speed photometry to search for evidence of fast rotation. We use these observations to obtain, for the first time, a reliable merger rate estimate for ultramassive white dwarfs. We present the details of our follow-up observations in Section 2, model atmosphere analysis in Section 3, and the constraints on photometric variability in Section 4. We discuss the merger fraction of ultramassive white dwarfs in Section 5, along with the implications for the binary population synthesis models, and conclude in Section 6.

## 2 OBSERVATIONS

### 2.1 Spectroscopy

We obtained follow-up optical spectroscopy of 13 targets using the Gemini North and South 8m telescopes equipped with the Gemini Multi-Object Spectrograph (GMOS) as part of the queue programs GN-2022A-Q-303 and GS-2022A-Q-106. We used the B600 grating and a 1'' slit, providing wavelength coverage from 3670 Å to 6800 Å and a resolution of 2 Å per pixel in the 4 × 4 binned mode.

Two additional targets, J0329-2123 and J0426-5025, could not be observed at Gemini during the 2022A semester. We obtained spectra for these two targets at the 6.5m Magellan telescope with the MagE spectrograph. We used the 0.85'' slit, providing wavelength coverage from about 3400 Å to 9400 Å with a resolving power of  $R = 4800$ . To extend the wavelength coverage for one of our Gemini targets with an intriguing spectrum, J1819–1208, we obtained additional MagE observations that confirmed the hot DQ spectral classification.

### 2.2 High-cadence Photometry

We acquired high speed photometry of 15 of our targets between 2021 October and 2022 July using the APO 3.5m telescope with the Agile frame transfer camera (Mukadam et al. 2011) and the BG40 filter. We obtained back-to-back exposures of 10-30 s over 2 hours for most of the objects, but we were limited to ~1-1.5 hours of observation time for three targets, J1116–1603, J1140+2322, and J1329+2549. We binned the CCD by 2×2, which resulted in a plate scale of 0.258'' pixel<sup>-1</sup>.

We obtained simultaneous *g*- and *i*-band observations of four targets using the dual-channel frame-transfer camera Zorro on the Gemini South telescope as part of the program GS-2022A-Q-303. We obtained 10 s long back-to-back exposures of each target over an hour. Zorro provides imaging over a 60'' field of view in the wide-field mode with a plate scale of 0.07'' pixel<sup>-1</sup>.

We obtained additional time-series observations of two targets with the ProEm frame-transfer CCD on the McDonald Observatory 2.1m Otto Struve Telescope at Cassegrain focus. We used the BG40 filter with 15-20 s exposures.

Including the APO observations of the three magnetic white dwarfs from Kilic et al. (2021b), we have so far observed 20 of the 25 white dwarfs in our sample with the frame transfer cameras at the

APO, Gemini, and McDonald Observatory telescopes. Two additional targets have high-cadence photometry published in the literature (Pshirkov et al. 2020; Caiazzo et al. 2021). Hence, only three of our targets, J0049–2525, J0426–5025, and J1727+3831, currently lack follow-up high-speed photometry.

## 3 MODEL ATMOSPHERE ANALYSIS

### 3.1 The Fitting Method

Kilic et al. (2021a) provided model atmosphere fits to all 25 ultramassive white dwarfs with  $M \geq 1.3 M_{\odot}$  in the Montreal White Dwarf Database. However, they had spectroscopy available for only 10 of these targets. Here we revisit the model atmosphere analysis of the 15 targets with recently obtained Gemini and Magellan follow-up spectroscopy.

We use the photometric technique, and use the SDSS *u* and Pan-STARRS *grizy* photometry along with the Gaia EDR3 parallaxes to constrain the effective temperature and the solid angle,  $\pi(R/D)^2$ , where  $R$  is the radius of the star and  $D$  is its distance. Given precise distance measurements from Gaia, we constrain the radius of each star directly, and therefore its mass based on the evolutionary models for a given core composition. The details of our fitting method, including the model grids used are further discussed in Bergeron et al. (2019), Genest-Beaulieu & Bergeron (2019), Blouin et al. (2019), and Kilic et al. (2020, 2021a).

### 3.2 DA White Dwarfs

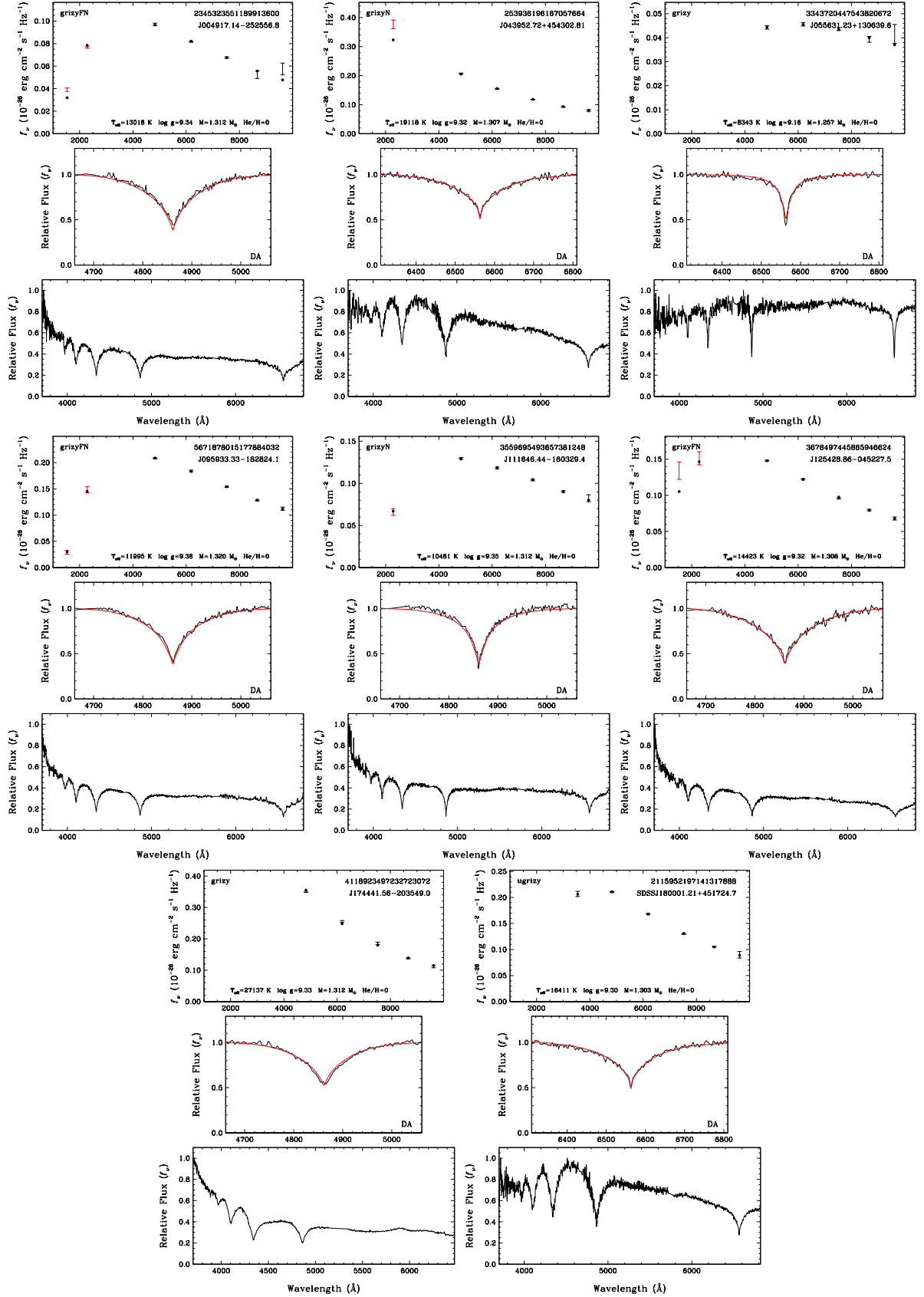
Figure 1 shows our model fits for eight ultramassive DA white dwarfs observed at Gemini. For each star, the top panel shows the available SDSS *u*, Pan-STARRS *grizy*, and GALEX FUV and NUV photometry (error bars) along with the predicted fluxes from the best-fitting pure hydrogen atmosphere models (filled dots). The labels in the same panel give the Gaia DR2 Source ID, object name, and the photometry used in the fitting. The middle panel shows the predicted spectrum based on the pure hydrogen solution, along with the observed  $H\alpha$  or  $H\beta$  line profiles.

We simply over-plot the predicted hydrogen line profile (red line) from the photometric fit to see if a given spectrum is consistent with a pure hydrogen atmosphere composition, and in all cases here that is the case. The bottom panel shows the entire Gemini GMOS spectrum of each object. We confirm seven of these objects as ultramassive DA white dwarfs with  $T_{\text{eff}} > 10,000$  K and  $M \geq 1.3 M_{\odot}$ , assuming a CO core. The exception is J0556+1306, which is best explained by a pure H atmosphere white dwarf with  $T_{\text{eff}} = 8340 \pm 260$  K and  $M = 1.257 \pm 0.023 M_{\odot}$ .

### 3.3 A Hot DQ White Dwarf

Figure 2 shows our model fits to J1819–1208, a unique object in our sample with no traces of hydrogen or helium lines in its spectrum. In fact, the optical spectrum of J1819–1208 is dominated by carbon and oxygen lines, making it a member of the hot DQ spectral type. Hot DQ white dwarfs with temperatures between about 18,000 and 24,000 K are unique in having atmospheres dominated by carbon and oxygen (Dufour et al. 2007, 2008).

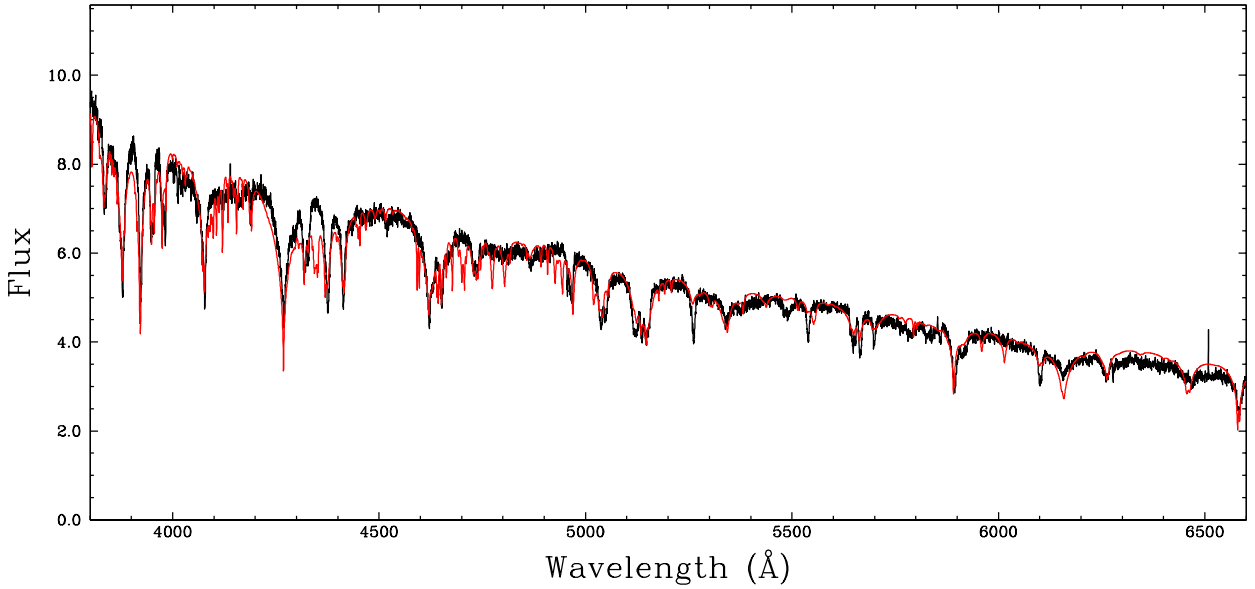
We rely on a new model atmosphere grid for hot DQ stars (see Dufour et al. 2011) with effective temperatures between 16,000 and 25,000 K for a fixed value of  $C/O = 1.0$  for this exploratory study. The details of these models will be presented in a future publication. We



**Figure 1.** Model atmosphere fits to eight ultramassive DA white dwarfs observed at Gemini. The top panels show the best-fitting H (filled dots) and He (open circles) atmosphere white dwarf models to the photometry (error bars), and includes the Gaia DR2 Source ID, object name, and the photometry used in the fitting: *ugrizyFN* means SDSS *u* + Pan-STARRS *grizy*, and Gaia FUV and NUV. The atmospheric parameters of the favored solution are highlighted in red. Here, and in the following figures, we show the model parameters for CO core white dwarfs. The middle panels show the observed spectrum (black line) along with the predicted spectrum (red line) based on the pure H atmosphere solution. The bottom panels show a broader wavelength range for each object.

**Table 1.** Physical Parameters of our Ultramassive White Dwarf Sample assuming ONe or CO cores. All solutions above  $1.29 M_{\odot}$  for ONe core models and above  $1.334 M_{\odot}$  for CO core models are extrapolated. The last 10 objects had spectroscopy available in the literature prior to this work.

Object	Comp	Spectral Type	$T_{\text{eff}}$ (K)	ONe core Mass ( $M_{\odot}$ )	ONe core Cooling Age (Gyr)	CO core Mass ( $M_{\odot}$ )	CO core Cooling Age (Gyr)	Merger ?
J004917.14–252556.81	H	DA	$13020 \pm 460$	$1.263 \pm 0.011$	$1.94 \pm 0.08$	$1.312 \pm 0.010$	$1.72 \pm 0.09$	
J032900.79–212309.24	H	DAH	$10330 \pm 290$	$1.305 \pm 0.010$	$2.32 \pm 0.06$	$1.344 \pm 0.008$	$1.87 \pm 0.09$	✓
J042642.02–502555.21	H	DAH	$17900 \pm 1570$	$1.264 \pm 0.019$	$1.30 \pm 0.16$	$1.312 \pm 0.016$	$1.08 \pm 0.16$	✓
J043952.72+454302.81	H	DA	$19120 \pm 630$	$1.258 \pm 0.008$	$1.18 \pm 0.06$	$1.307 \pm 0.007$	$0.96 \pm 0.06$	
J055631.17+130639.78	H	DA	$8340 \pm 260$	$1.207 \pm 0.021$	$3.33 \pm 0.12$	$1.257 \pm 0.023$	$3.34 \pm 0.18$	
J060853.60–451533.03	H	DC/DAH	$19580 \pm 1910$	$1.258 \pm 0.021$	$1.13 \pm 0.16$	$1.307 \pm 0.019$	$0.92 \pm 0.17$	✓
J070753.00+561200.25	H	DC/DAH	$18100 \pm 350$	$1.240 \pm 0.005$	$1.23 \pm 0.04$	$1.291 \pm 0.005$	$1.06 \pm 0.04$	✓
J080502.93–170216.57	H	DAH	$10830 \pm 110$	$1.254 \pm 0.004$	$2.40 \pm 0.03$	$1.304 \pm 0.003$	$2.20 \pm 0.03$	✓
...	[H/He]=–5	...	$10010 \pm 120$	$1.213 \pm 0.004$	$2.70 \pm 0.04$	$1.249 \pm 0.006$	$2.23 \pm 0.04$	
J093430.71–762614.48	H	DAH	$10050 \pm 1350$	$1.284 \pm 0.055$	$2.47 \pm 0.35$	$1.328 \pm 0.047$	$2.11 \pm 0.50$	✓
...	[H/He]=–5	...	$9180 \pm 1050$	$1.238 \pm 0.052$	$2.86 \pm 0.33$	$1.279 \pm 0.051$	$2.32 \pm 0.46$	
J095933.33–182824.16	H	DA	$12000 \pm 180$	$1.273 \pm 0.005$	$2.12 \pm 0.03$	$1.320 \pm 0.004$	$1.83 \pm 0.04$	
J111646.44–160329.42	H	DA	$10480 \pm 170$	$1.264 \pm 0.007$	$2.45 \pm 0.05$	$1.312 \pm 0.006$	$2.21 \pm 0.07$	✓
J125428.86–045227.48	H	DA	$14420 \pm 390$	$1.258 \pm 0.008$	$1.71 \pm 0.06$	$1.308 \pm 0.007$	$1.52 \pm 0.06$	
J174441.56–203549.05	H	DA	$27140 \pm 890$	$1.271 \pm 0.008$	$0.65 \pm 0.06$	$1.312 \pm 0.008$	$0.43 \pm 0.04$	
J180001.21+451724.7	H	DA	$16410 \pm 290$	$1.253 \pm 0.003$	$1.44 \pm 0.03$	$1.303 \pm 0.004$	$1.26 \pm 0.04$	
J181913.36–120856.44	C/O	hotDQ	23800	...	...	1.243	0.42	✓
J010338.56–052251.96	H	DAH:	$9040 \pm 70$	$1.262 \pm 0.003$	$2.84 \pm 0.03$	$1.310 \pm 0.003$	$2.60 \pm 0.04$	✓
J025431.45+301935.38	[H/He]=–5	DC	$11060 \pm 560$	$1.302 \pm 0.024$	$2.25 \pm 0.10$	$1.330 \pm 0.016$	$1.49 \pm 0.17$	
...	[C/He]=–4	...	$10190 \pm 290$	$1.261 \pm 0.016$	$2.53 \pm 0.08$	$1.301 \pm 0.014$	$1.93 \pm 0.12$	
J114012.81+232204.7	H	DA	$11860 \pm 220$	$1.294 \pm 0.008$	$2.10 \pm 0.04$	$1.336 \pm 0.006$	$1.71 \pm 0.06$	
J132926.04+254936.4	H	DA	$29010 \pm 750$	$1.314 \pm 0.006$	$0.81 \pm 0.05$	$1.351 \pm 0.006$	$0.37 \pm 0.03$	
J172736.28+383116.9	H	DA	$9420 \pm 200$	$1.252 \pm 0.012$	$2.78 \pm 0.08$	$1.302 \pm 0.011$	$2.59 \pm 0.12$	
J183202.83+085636.24	He	DBA	$34210 \pm 1020$	$1.301 \pm 0.006$	$0.45 \pm 0.03$	$1.319 \pm 0.004$	$0.20 \pm 0.02$	✓
J190132.74+145807.18	H	DC/DAH	$29100 \pm 480$	$1.279 \pm 0.003$	$0.61 \pm 0.02$	$1.319 \pm 0.004$	$0.35 \pm 0.02$	✓
J221141.80+113604.5	[H/He]=–1.5	DAH	7500 - 8390	$1.231 \pm 0.010$	3.1 - 3.2	$1.268 \pm 0.010$	2.6 - 2.9	✓
J225513.48+071000.9	H	DC/DAH	$10990 \pm 210$	$1.252 \pm 0.012$	$2.36 \pm 0.05$	$1.302 \pm 0.011$	$2.18 \pm 0.09$	✓
J235232.30–025309.2	H	DA	$10680 \pm 100$	$1.272 \pm 0.003$	$2.38 \pm 0.02$	$1.319 \pm 0.003$	$2.10 \pm 0.03$	✓

**Figure 2.** Model atmosphere fit to the hot DQ white dwarf J1819–1208 assuming equal amounts of carbon and oxygen in the atmosphere. The best-fitting effective temperature is 23800 K.

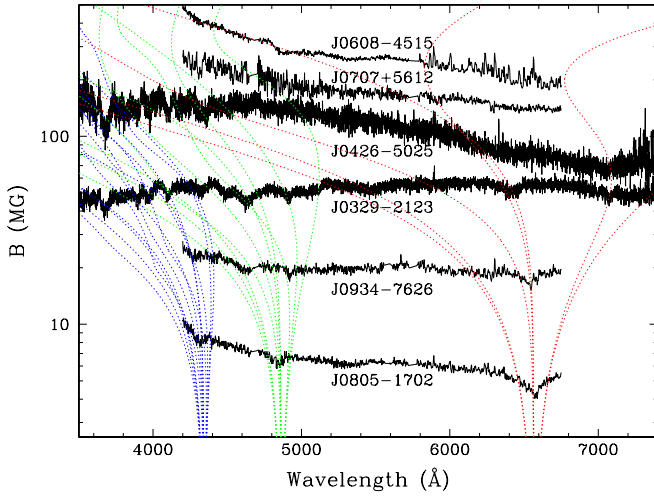


**Figure 3.** Spectra of six newly identified magnetic white dwarfs compared to predicted line positions of  $H\alpha$ ,  $H\beta$ , and  $H\gamma$  as a function of the magnetic field strength (Schimeczek & Wunner 2014). The bottom three objects, J0805–1702, J0934–7626, and J0329–2123 have  $B \sim 5, 25$ , and  $50$  MG, respectively. The remaining three objects are strongly magnetic, but it is difficult to constrain their field strength based on the available data.

fixed the surface gravity to  $\log g = 9.0$  and fitted for the effective temperature. The best-fitting model has  $T_{\text{eff}} = 23,800$  K and is shown in red in Figure 2. This model does a decent job of matching the spectral features in the spectrum of J1819–1208, though some of the oxygen lines are weaker than predicted by this model, indicating that the oxygen to carbon ratio is likely smaller than one. We defer a detailed model atmosphere analysis of this object to a future publication, but confirm that J1819–1208 is a relatively hot DQ white dwarf with a carbon and oxygen atmosphere. Fixing the effective temperature at  $23,800$  K, the spectral energy distribution of J1819–1208 based on Pan-STARRS photometry and Gaia parallax indicates a mass of  $1.24 M_{\odot}$  and a cooling age of  $420$  Myr.

### 3.4 Magnetic White Dwarfs

Six of the newly observed ultramassive white dwarfs are magnetic. Figure 3 shows the Gemini and Magellan spectra of these six targets along with the predicted Zeeman components of  $H\alpha$ ,  $H\beta$ , and  $H\gamma$  as a function of the magnetic field strength from Schimeczek & Wunner (2014). Two of these targets, J0805–1702 and J0934–7626 show  $H\alpha$  near its rest wavelength, and are compatible with  $B \sim 5$ – $25$  MG fields (see below). Two other targets, J0329–2123 and J0426–5025, show several absorption features in the blue that likely require  $B \sim 50$ – $100$  MG fields. Yet two other targets, J0608–4515 and J0707+5612, show essentially featureless spectra, but have effective temperatures near  $18,000$ – $20,000$  K based on their overall spectral energy distributions. Hence, the only way for them to have featureless spectra is if they are strongly magnetic. Fitting the spectra of these strongly magnetic white dwarfs is beyond the scope of this paper, and their location in Figure 3 is arbitrary and should not be taken as an indication of their actual magnetic field strengths.

For J0805–1702 and J0934–7626, the two magnetic white dwarfs where  $H\alpha$  and  $H\beta$  are clearly visible, we computed magnetic model spectra using an approach similar to that described in Bergeron et al. (1992) and Kilic et al. (2021b). We use offset dipole models, where the independent parameters are the dipole field strength  $B_d$ , the

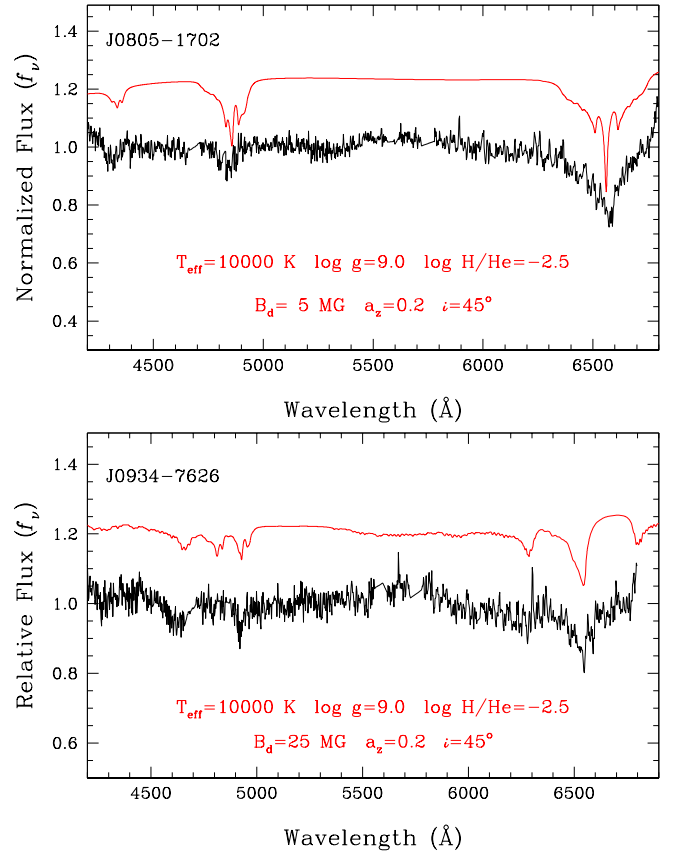


**Figure 4.** A comparison between the observed Gemini spectra of the magnetic DA white dwarfs J0805–1702 and J0934–7626 and a mixed H/He atmosphere white dwarf model with  $T_{\text{eff}} = 10,000$  K,  $\log g = 9$ ,  $\log \text{H/He} = -2.5$ , a dipole field strength of  $B_d = 5$  MG (for J0805–1702) and  $25$  MG (for J0934–7626), the dipole offset  $a_z = 0.2$ , and a viewing angle of  $i = 45^\circ$ .

dipole offset  $a_z$  measured in units of stellar radius from the center of the star, and the viewing angle  $i$  between the dipole axis and the line of sight ( $i = 0^\circ$  for a pole-on view).

The best-fitting models under the assumption of a pure hydrogen composition for these two stars require the Balmer lines to be stronger than observed, regardless of the field strength and geometry. One way to reduce the strength of the Balmer lines is if these stars have mixed hydrogen and helium atmospheres, similar to the magnetic white dwarf J2211+1136 (Kilic et al. 2021b). Figure 4 shows a comparison of the observed spectra of J0805–1702 and J0934–7626 with a model where  $T_{\text{eff}} = 10,000$  K,  $\log g = 9$ ,  $\log \text{H/He} = -2.5$ ,  $B_d = 5$  MG (for J0805–1702) and  $25$  MG (for J0934–7626),  $a_z = 0.2$ , and  $i = 45^\circ$ . Note that the model shown in each panel is not a fit. We simply overplot these models to demonstrate that 1) both J0805–1702 and J0934–7626 have mixed hydrogen and helium atmospheres, and 2) they have field strengths of  $\sim 5$  and  $25$  MG, respectively.

Table 1 presents the physical parameters of all 25 ultramassive white dwarfs in our sample. For completeness, we provide the masses and the cooling ages for both ONe and CO core compositions. Table 1 also includes the 10 objects with spectroscopy analyzed in Kilic et al. (2021a,b) at the bottom, which includes 3 objects classified as DC. However, only one of these objects, J0254+3019, is a genuine DC white dwarf with no clear evidence of magnetism. The other two, J1901+1458 and J2255+0710, show broad shifted Zeeman absorption features that indicate a strong magnetic field (Caiazzo et al.

2021; Kilic et al. 2021b). Interestingly, 10 out of the 25 white dwarfs in our sample show evidence of magnetism in their optical spectra. This is about a factor of four higher than the fraction of magnetic white dwarfs within the local 20 pc sample (Holberg et al. 2016). Note that our low-resolution spectroscopy is not sensitive to fields strengths below about 100 kG. Hence, there may be other magnetic white dwarfs with weaker fields hiding in the sample.

#### 4 VARIABILITY

Short period photometric variability on minute timescales in single white dwarfs occur due to two main reasons; pulsation or rapid rotation. Depending on the main atmospheric constituent, white dwarfs pulsate at effective temperatures near 25,000 K if they have pure helium atmospheres (Winget et al. 1982; Vanderbosch et al. 2022) and 12,000 K if they have pure hydrogen atmospheres (e.g., Tremblay et al. 2015). The most massive DAV pulsators currently known, BPM 37093 (Kanaan et al. 1992) and GD 518 (Hermes et al. 2013) have  $M \approx 1.1 M_{\odot}$  (Bédard et al. 2017; Kilic et al. 2020), and they show multi-periodic oscillations with periods between 400 and 600 s.

Our ultramassive white dwarf sample includes 10 magnetic white dwarfs. Brinkworth et al. (2013) discovered photometric variability in 67% of the isolated magnetic white dwarfs in their sample, with periods as short as 27 minutes. Hence, a significant fraction of the ultramassive white dwarfs in our sample may show photometric variability due to rapid rotation. In fact, five of our targets (one DBA and 4 magnetic DAH spectral types) have high-cadence time-series observations available in the literature, and three show variability at 70 s, 5.88 min, and 6.94 min (Kilic et al. 2021b; Pshirkov et al. 2020; Caiazzo et al. 2021). Here we present the results from a search for rapid rotation in the rest of the sample using time-series observations. We discuss the non-variable objects first, and then present newly discovered rapidly rotating systems, and other potentially variable objects.

##### 4.1 Nonvariables

Figure 5 shows the APO 3.5m light-curves and their Fourier transforms for 12 targets that were not observed to vary at minute timescales. The dotted lines mark the  $4\langle A \rangle$  level, where  $\langle A \rangle$  is the average amplitude in the Fourier transform. Depending on the source brightness and the sky conditions, this limit ranges from 2 millimag in the best case, for J1819–1208, to 20 millimag in the worst case, for J0254+3019. The latter is not ideal, and follow-up observations would be useful to search for low-level variability in J0254+3019 and similar targets. Our observations typically span two hours, and therefore they do not provide any constraints on the longer timescale variability of these white dwarfs. Eight of these objects have  $g$ -band photometry available in the ZTF Data Release 12, but the ZTF data do not reveal any significant variations either.

Two of the photometrically non-variable objects shown in Figure 5, J0805–1702 and J2255+0710, are magnetic. Kilic et al. (2021b) presented high speed photometry of the latter target over an hour, and ruled out variability at the 16 mmag level. The new data presented here expand the time baseline to 2 hours and provides more stringent results on the variability in this system, ruling out variability at 7 mmag and higher.

Figure 6 shows the light curves and their Fourier transforms for three additional targets observed at the Gemini South telescope with the Zorro instrument. Each object was observed over an hour, and

the Zorro field of view included at least two reference stars that are significantly redder than the target white dwarfs. All three stars show a peak in the Fourier transform, usually below the  $4\langle A \rangle$  level, at low frequencies due to our observing window and differential extinction. J0608–4515 shows the strongest signal at exactly 24 cycles/day and its harmonics. The bottom left panel in Figure 6 includes the Fourier transform of one of the reference stars, which also shows a significant peak at low frequencies, similar to J0608–4515. Hence, we classify J0608–4515 and the other two objects shown here as non-variable. J0608–4515 was also observed as part of the Catalina Sky Survey. The Catalina data also do not show any large scale variability, though the photometry is relatively noisy for this star with median errors of 0.2 mag.

##### 4.2 Rapid Rotators

We detect evidence of fast rotation in two of our targets, both of which are magnetic. The first, J0707+5612, is a  $T_{\text{eff}} = 18100 \pm 350$  K and  $M = 1.29 M_{\odot}$  (assuming a CO core) white dwarf with a featureless spectrum that requires strong magnetism to explain the observed spectra. It shows clear photometric variations in the ZTF data. The left panels in Figure 7 show the ZTF  $g$ -band light curve of J0707+5612 along with its Fourier transform, which shows a peak with  $20 \pm 2$  mmag amplitude at a frequency of  $22.80963 \pm 0.00004$  cycles per day (63 min period). The bottom left panel shows the light curve folded at this highest peak in the Fourier transform, along with the best-fitting sinusoidal model (red line).

We obtained follow-up BG-40 filter observations of J0707+5612 at both APO and McDonald telescopes. The middle and right panels in Figure 7 show the results of these observations. Our APO run was unfortunately limited to an hour, and it is therefore impossible to constrain the period of variation precisely based on these data. However, the Fourier transform of the APO data shows a broad peak that is consistent with the ZTF results. Our McDonald 2.1m observations span 2.9 hours, and display  $17 \pm 2$  mmag amplitude variations at a frequency of 24.66 cycles per day. Given that the McDonald data cover less than three rotation cycles, the period estimate is also uncertain. The ZTF data provide the best constraints on the rotation period of J0707+5612.

The second newly discovered rapid rotator is J0329–2123, which is also a magnetic DAH white dwarf with  $T_{\text{eff}} = 10330 \pm 290$  K and  $M = 1.34 M_{\odot}$  (assuming a CO core). These parameters put it outside of the ZZ Ceti instability strip (see below). Figure 8 shows our APO observations of J0329–2123 over two different nights. Each observation is 2 hours long. Observations on UT 2021 Oct 9 (left panels) show two significant frequencies: the main peak at  $154.1 \pm 1.2$  cycles per day (or 9.3 min) with  $8.3 \pm 1.4$  mmag amplitude and its harmonic at  $307.3 \pm 1.2$  cycles per day with  $7.8 \pm 1.4$  mmag amplitude. Both of these peaks are detected at the  $4\langle A \rangle$  level.

The right panels in Figure 8 show the data from UT 2021 Dec 2, with a slightly higher noise level in the Fourier transform. There is a peak at  $150.2 \pm 1.3$  cycles per day with  $7.7 \pm 1.5$  mmag at slightly below the  $4\langle A \rangle$  level, and its first harmonic is detected at  $303.8 \pm 1.7$  cycles per day with  $6.1 \pm 1.5$  mmag amplitude. Given the different signal-to-noise ratios of the light curves from each night, some of these frequencies fall below the  $4\langle A \rangle$  level, but they are persistent, and therefore likely to be real. Follow-up observations would be useful to confirm the low-level variability seen in this system, and confirm its rotation period of  $\sim 9.3$  min.

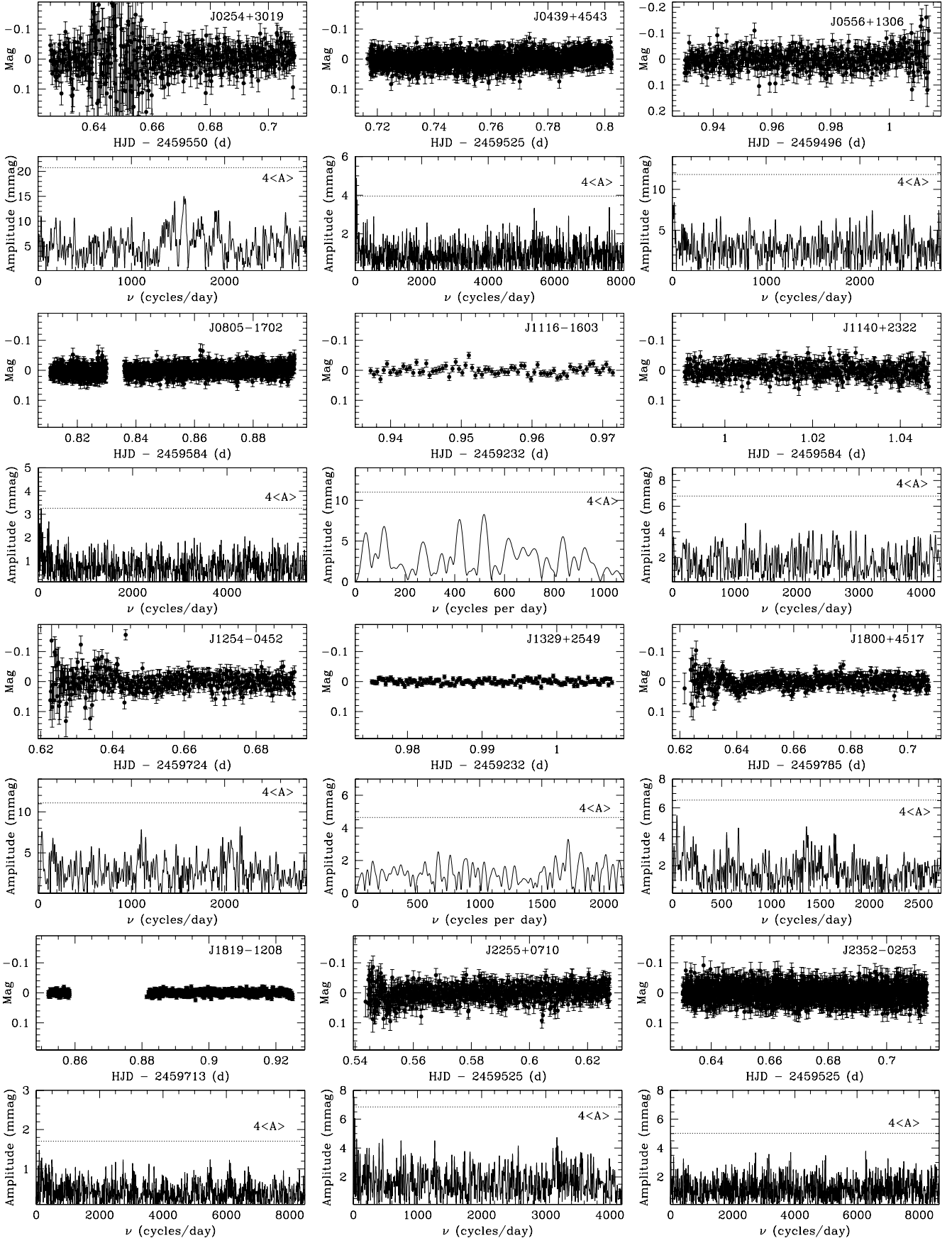


**Figure 5.** Light curves (top) and their Fourier transforms (bottom) of 12 non-variable white dwarfs observed at the APO 3.5m telescope. The dotted lines mark the  $4\langle A \rangle$  level, where  $\langle A \rangle$  is the average amplitude in the Fourier transform.

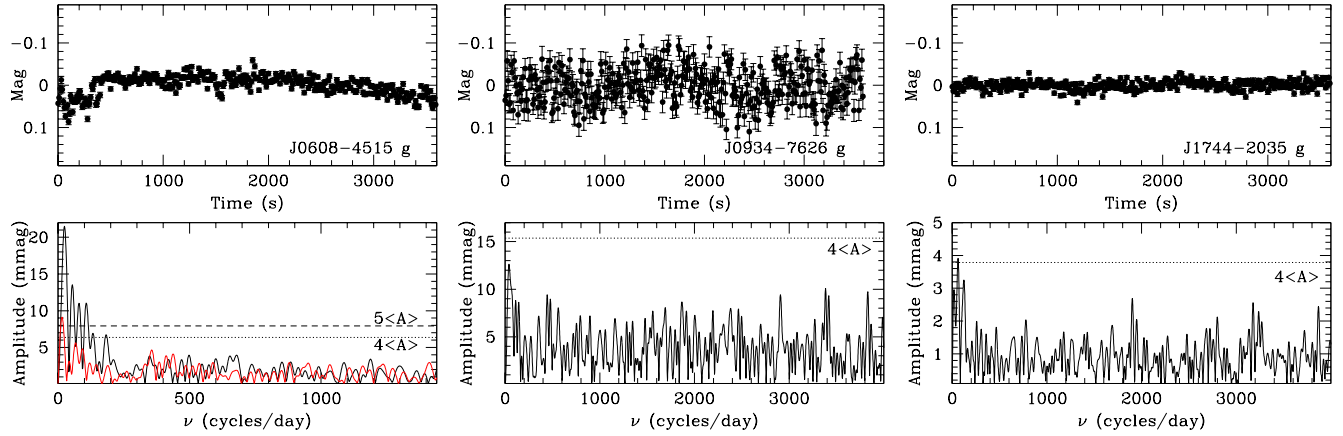


**Figure 6.** Light curves (top) and their Fourier transforms (bottom) of three white dwarfs observed at the Gemini South telescope with the Zorro instrument. The dotted and dashed lines show the 4 and 5<A> level, respectively. The red line in the bottom panel for J0608–4515 shows the Fourier transform of one of the reference stars in the Zorro field of view.

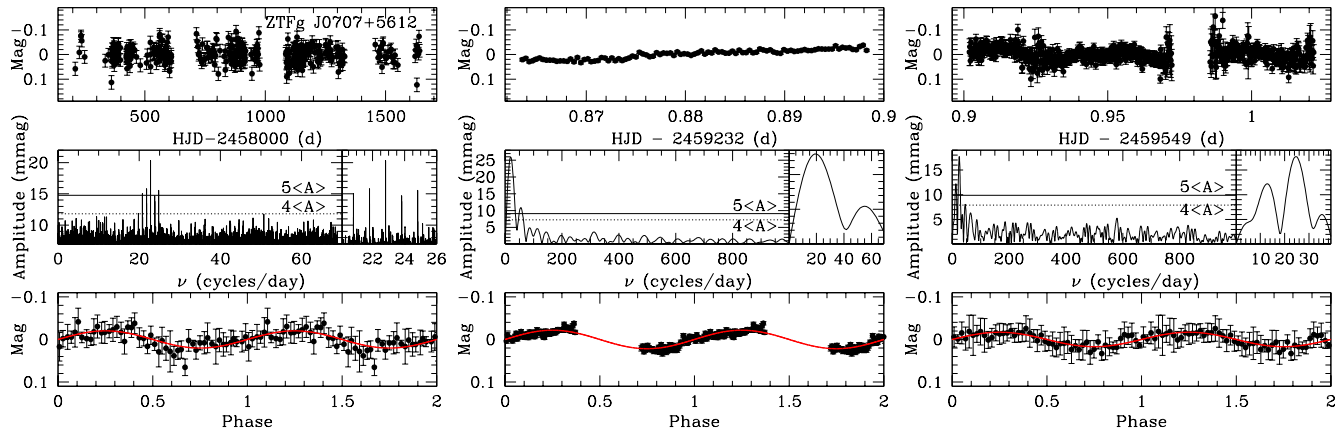


**Figure 7.** ZTF (left), APO (middle), and McDonald (right) light curves of the magnetic white dwarf J0707+5612. ZTF frequency  $22.80963 \pm 0.00004$  cycles/day with  $20 \pm 2$  mmag amplitude. McDonald frequency 24.66 cycles/day with  $17 \pm 2$  mmag amplitude, and APO frequency 18.7 cycles/day with  $22 \pm 1$  mmag amplitude.

### 4.3 Ultramassive ZZ Ceti Candidates

Our ultramassive white dwarf sample includes several objects near the ZZ Ceti instability strip. Even though the main goal in this study is not to search for massive pulsating white dwarfs, for completeness we discuss our observations of the DA white dwarfs near the instability strip.

Figure 9 shows the ZZ Ceti instability strip for DA white dwarfs using the 100 pc MWDD white dwarf sample (Dufour et al. 2017). Blue stars mark the previously known pulsating DAV white dwarfs in that sample, and the solid lines show the empirical boundaries of the instability strip from Tremblay et al. (2015). Spectroscopically confirmed DA, DC, and magnetic white dwarfs in our sample are marked by filled circles, open, and filled triangles, respectively. The DA white dwarfs near the boundaries of the instability strip are labeled. There are essentially four DA white dwarfs in our sample that are near the strip: J0049–2525, J0959–1828, J1140+2322, and J1254–0452.

J0049–2525 is by far the best ZZ Ceti candidate in our sample. It was included in our Gemini South observing program, but unfortunately the high speed photometry component did not get executed in the queue. J1140+2322 and J1254–0452 were observed at APO, and

their light curves are included in Figure 5. These stars were observed not to vary down to approximately 7 and 11 mmag level, respectively. The last object in this list, J0959–1828, is near the red edge of the instability strip.

We obtained follow-up observations of J0959–1828 on five different nights at the APO 3.5m, McDonald 2.1m, and Gemini South telescopes, with observations spanning one to two hours for APO, one hour for Gemini, and more than four hours for McDonald. Figure 10 shows all of the light curves for this system. The first night’s APO data shows a potential peak near 400 cycles  $d^{-1}$  (top left panels). This peak and another near 450 cycles  $d^{-1}$  is detected at the 4(A) level in the second night’s data (top middle panels) as well. However, the data from our third APO night (top right panels) do not show any significant variability. Longer baseline observations at the McDonald 2.1m also shows a potential peak near 400 cycles  $d^{-1}$ , but again this peak is below the 4(A) level in the Fourier transform.

Combining all of the APO and McDonald 2.1m, we detect two frequency peaks in the Fourier transform at  $402.7 \pm 0.1$  cycles  $d^{-1}$  with  $4.9 \pm 0.7$  mmag amplitude and  $446.4 \pm 0.5$  cycles  $d^{-1}$  with  $4.4 \pm 0.9$  mmag amplitude. These are detected at the 4(A) level in the combined data. On the other hand, our follow-up Gemini Zorro photometry (bottom right panels) do not show these frequency peaks



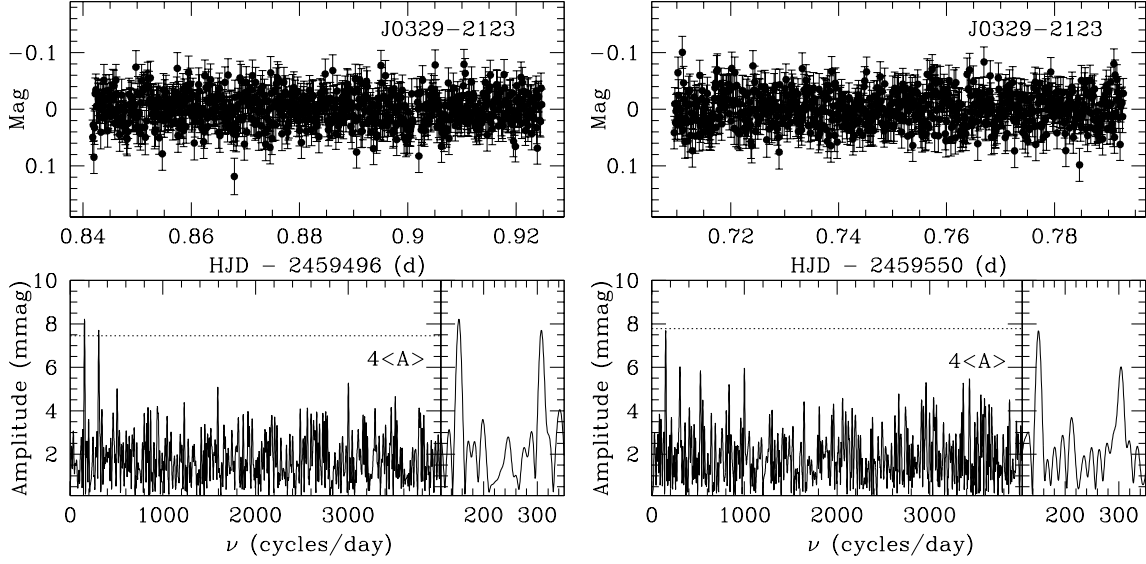


**Figure 8.** APO time-series photometry of the magnetic white dwarf J0329–2123 on two separate nights (top panels). The bottom panels show the Fourier transform of each light curve. The dotted lines show the  $4\langle A \rangle$  level.

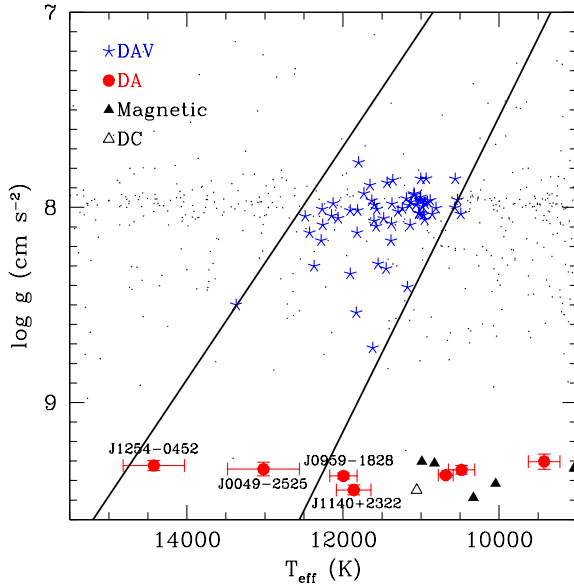


**Figure 9.** Temperatures and surface gravities of the 100 pc sample in the Montreal White Dwarf Database (Dufour et al. 2017). Blue stars mark the previously known pulsating DAV white dwarfs, and the solid lines mark the boundaries of the ZZ Ceti instability strip (Tremblay et al. 2015). Filled circles, open triangles, and filled triangles mark the DA, DC, and magnetic white dwarfs in our sample.

in the Fourier transform. Hence, we find these data inconclusive in terms of confirming variability in J0959–1828. It is relatively difficult to confirm the potential low-level variability of 4–5 mmag in this system from ground-based observations at 2–3 m class telescopes. Follow-up time-series photometry on 8m class telescopes or space-based telescopes would be helpful in confirming any potential variability in J0959–1828.

## 5 DISCUSSION

### 5.1 The Merger Fraction of Ultramassive White dwarfs

We searched for merger products among the 25 ultramassive white dwarfs with  $M \geq 1.3 M_{\odot}$  identified by Kilic et al. (2021a). We used three main methods for this; we searched for evidence of magnetism through optical spectroscopy, evidence of rapid rotation through high cadence photometry, and evidence of unusual kinematics through Gaia astrometry. Figure 11 shows a Venn diagram comparing the detection of magnetism, rapid rotation, and large tangential velocities in individual objects.

Our follow-up spectroscopy shows that 10 of these 25 objects are strongly magnetic, with field strengths of 5 MG or higher. This fraction, 40%, is a factor of four higher than observed in the local 20–25 pc white dwarf sample (Holberg et al. 2016; Hollands et al. 2018), and is telling about the origin of these ultramassive white dwarfs.

Isern et al. (2017) discussed the origin of magnetism in white dwarfs and proposed that in addition to the commonly invoked fossil fields and binary interactions, magnetic fields can also arise during core crystallization (see the review by Ferrario et al. 2020). In this scenario, the crystallization of a C/O core white dwarf and the ensuing phase separation leads to the formation of a convective mantle on top of a solid core. This convective region can produce a dynamo with magnetic field strengths of up to 0.1 MG. All three scenarios may be needed to explain the frequency of magnetic white dwarfs in volume limited white dwarf samples. However, the fossil fields and the crystallization scenarios are clearly inadequate for explaining the rapidly rotating and strongly magnetic ( $B \geq 5$  MG) ultramassive white dwarfs in our sample. García-Berro et al. (2012) demonstrated that the hot, convective, and differentially rotating corona present in the outer layers of a merger remnant can produce strong magnetic fields (see also Tout et al. 2008; Briggs et al. 2015), and such objects are expected to rotate on  $\sim$ minute timescales (Schwab 2021).

Our high cadence observations at APO, McDonald, and Gemini identified two additional rapidly rotating white dwarfs that are also strongly magnetic. J0707+5612 and J0329–2123 show photometric variability with periods of 63 min and  $\approx$  9.3 min, respectively. These

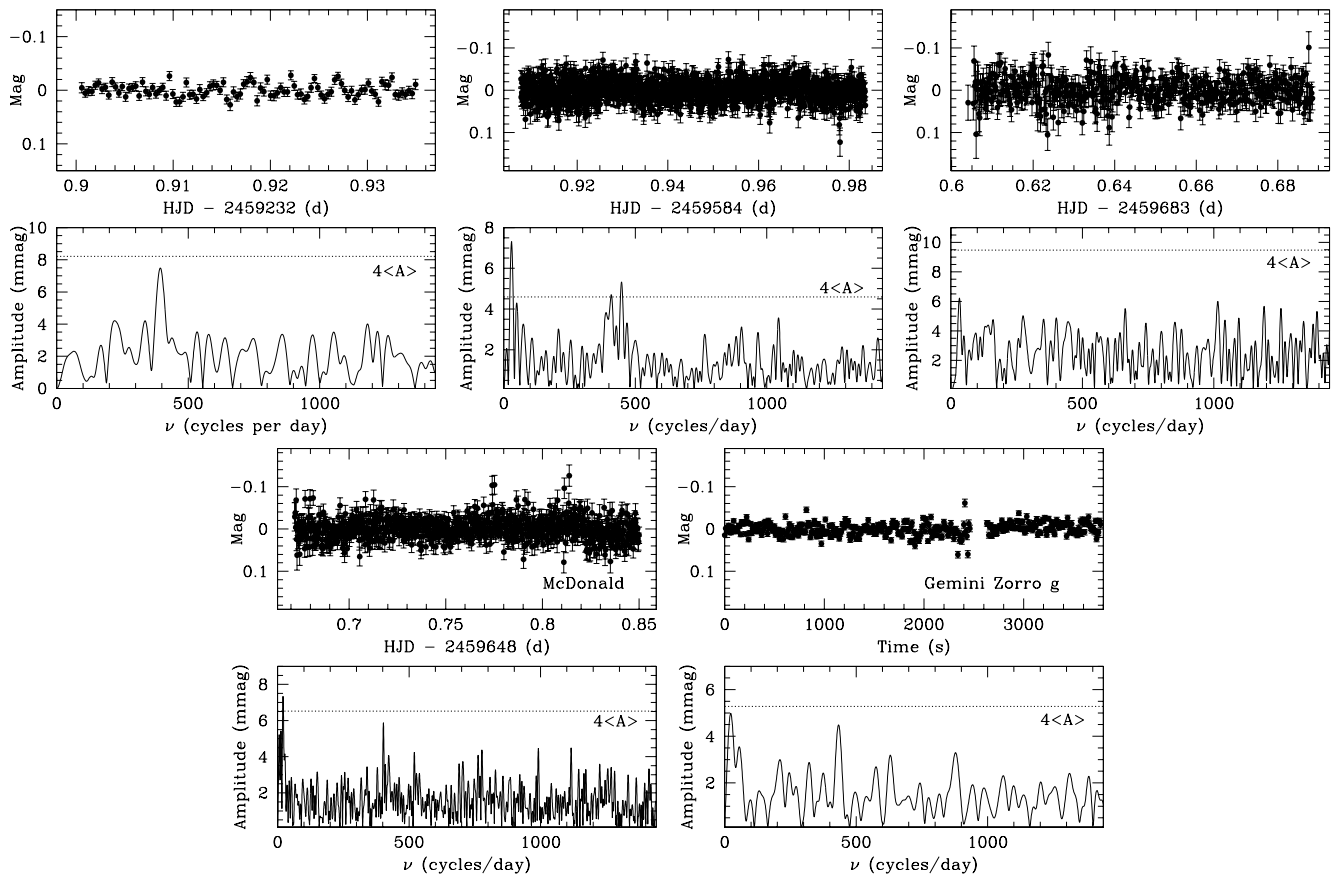


**Figure 10.** APO (top panels), McDonald 2.1m (bottom left panels), and Gemini Zorro (bottom right panels) time-series photometry of J0959–1828 on five different nights. The dotted lines show the  $4\langle A \rangle$  level in the Fourier transforms.

are much faster than the typical day long rotation rates observed in average mass ( $M \sim 0.6 M_{\odot}$ ) pulsating white dwarfs (Hermes et al. 2017), but they are consistent with the expectations for white dwarf merger products (Schwab 2021). There are three other rapidly rotating white dwarfs known in our sample, J1832+0856, J1901+1458, and J2211+1136 (Pshirkov et al. 2020; Caiazzo et al. 2021; Kilic et al. 2021b), bringing the total number of rapidly rotating objects in our sample to five. Hence, 20% of the most massive white dwarfs in the Montreal White Dwarf Database 100 pc sample rotate with periods ranging from roughly 1 min to 1 hour.

Kinematics provide another way to identify white dwarfs with unusual evolutionary histories. Binary interactions and mergers can reset the evolutionary clock of a white dwarf progenitor and make its descendant white dwarf appear younger and hotter than what it would be if it went through single star evolution. Our ultramassive white dwarf sample consists of objects with relatively young cooling ages of  $\sim 1$  Gyr. Hence, they should, on average, show disk kinematics. Kilic et al. (2021a) identified four outliers in tangential velocity. Even though the average tangential velocity of the sample,  $21 \text{ km s}^{-1}$ , is consistent with a young disk population, they found four objects with  $V_{\text{tan}} > 50 \text{ km s}^{-1}$ . These four objects, J0805–1702, J1116–1603, J2211+1136, and J2352–0253, likely suffered from binary interactions and mergers in the past.

Five objects show more than one symptom of being a merger product. Out of the 10 magnetic white dwarfs in our sample, four are also fast rotators, and two display large tangential velocities. Namely, J0329–2123, J0707+5612, and J1901+1458 are rapidly ro-

tating, magnetic ultramassive massive white dwarfs. J0805–1702 is a magnetic ultramassive white dwarf with an unusually large tangential velocity of  $90 \text{ km s}^{-1}$ . J2211+1136 is the best example of a merger product. It is a  $1.27 M_{\odot}$  white dwarf with a  $B = 15 \text{ MG}$  field, a rotation period of only 70 s, and a relatively large tangential velocity of  $56 \text{ km s}^{-1}$ .

The Venn diagram in Figure 11 excludes the normal DA and DC white dwarfs in our sample. However, there is one more object that is likely a merger product, but it is excluded from this figure because it does not show any obvious evidence of magnetism, rapid rotation, or a large tangential velocity. The hot DQ white dwarf J1819–1208 is likely a merger product based on its unusual composition and the overall properties of the hot DQ population in the solar neighborhood. More than 70% of the hot DQs are magnetic, and at least one third of these stars are also variable (e.g., Montgomery et al. 2008; Dufour et al. 2011). Dunlap & Clemens (2015) argued that the unique atmospheric compositions, high masses, high incidence of magnetism, and relatively high tangential velocities favor a merger origin for hot DQ white dwarfs. Williams et al. (2016) demonstrate that the photometric variability in these objects is likely due to rotation, and that hot DQ white dwarfs contain many rapid rotators. Our time-series photometry on J1819–1208 did not reveal short period variability, but our observations are not sensitive to hour or day long periods. Hence, the unusual atmospheric composition of J1819–1208 makes it a prime candidate for a merger product.

Adding J1819–1208 to the list of 13 objects shown in Figure 11 brings the total number of merger products among our ultramassive

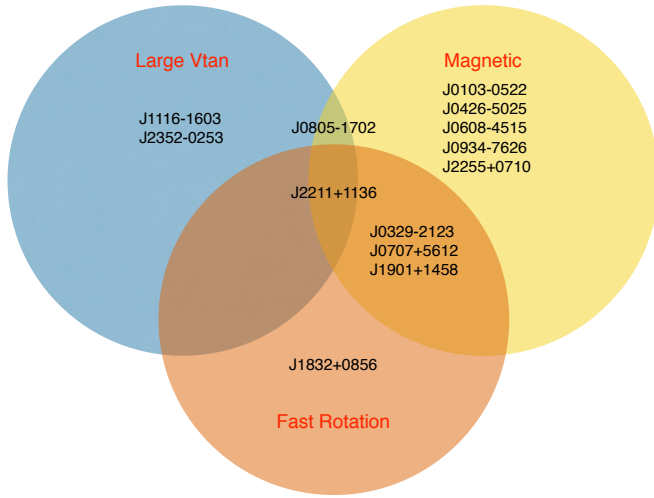


**Figure 11.** Venn diagram comparing the detection of magnetism, rapid rotation, and large tangential velocities in individual objects. Five targets show more than one symptom of being a merger product, and one object, J2211+1136, shows all three symptoms.

white dwarf sample to 14, which is remarkable. We use the binomial probability distribution to compute the upper and lower limits on the frequency of mergers (Burgasser et al. 2003). Since this probability function is not symmetric about its maximum value, we report the range in probability that delimits 68% of the integrated probability function, equivalent to  $1\sigma$  Gaussian limits. Since 14 of the 25 of our targets show evidence of a merger origin, this corresponds to a merger fraction of  $56_{-10}^{+9}\%$ , and a two sigma lower limit of 36.6%.

## 5.2 Binary Population Synthesis Predictions

From binary population synthesis calculations, Temmink et al. (2020) estimated that 10 to 30% of all observable single white dwarfs are formed through binary mergers, where the primary contribution is from the mergers between a post-main-sequence star and a main-sequence star<sup>1</sup>. Mergers provide a more significant contribution to single massive white dwarfs. For masses above  $0.9 M_{\odot}$  mergers contribute 30 to 45% of all observable single white dwarfs within 100 pc, where the dominant contribution is from double white dwarf mergers in most models.

The outcome of the binary population synthesis calculations depends heavily on the input assumptions for the binary physics and initial conditions (e.g. the ranges in the fractions mentioned above). One of the most important assumptions for the formation of compact binaries and mergers involve the common envelope phase. The  $\alpha$  prescription (Webbink 1984) is most commonly used to model it, where  $\alpha$  represents the fraction of the orbital energy that is used to unbind the common envelope. An additional dimensionless parameter  $\lambda$  (de Kool et al. 1987), which depends on the structure of the donor star, is also used in this prescription (Nelemans et al. 2000; Temmink et al. 2020).  $\alpha$  and  $\lambda$  are often treated as a single parameter  $\alpha\lambda$  since the product of the two parameters,  $\alpha\lambda$ , appears naturally in solutions for the orbital separation of the binary system after the common envelope evolution. In the fiducial model of Temmink et al.

(2020), they adopt  $\alpha\lambda = 2$  based on the reconstruction of the evolution of double helium white dwarfs by Nelemans et al. (2000). They also tested the sensitivity of their models to a less efficient and a more efficient common envelope phase by assuming  $\alpha\lambda = 0.25$  and  $\alpha\lambda = 5$ , respectively<sup>2</sup>.

Figure 9 in Temmink et al. (2020) shows the merger fraction as a function of mass based on binary population synthesis calculations using six different prescriptions (the default model, efficient  $\alpha$ , and inefficient  $\alpha$ , etc). The largest difference in the predicted merger fraction is indeed due to the adopted common envelope prescription. For example, the default model predicts a 37% merger rate for  $1.3 M_{\odot}$  white dwarfs, but this rate goes down to about 28% for an efficient common envelope with  $\alpha\lambda = 5$ , and it could be as high as 44% for an inefficient common envelope with  $\alpha\lambda = 0.25$ .

## 5.3 Implications for the Common-Envelope Evolution

The merger fraction of our ultramassive white dwarf sample with  $M \approx 1.3 M_{\odot}$  is  $56_{-10}^{+9}\%$ . This is higher than all of the predictions from the binary population synthesis calculations of Temmink et al. (2020), but it is consistent with the models using an inefficient (low) common envelope parameter within  $\approx 1\sigma$ . The default model in the population synthesis calculations is at the  $2\sigma$  lower limit of our measurement, and the calculations assuming an efficient common envelope evolution are at the  $3\sigma$  lower limit of our measurement. Hence, the observed merger fraction of our ultramassive white dwarf sample clearly favors low values of the common envelope efficiency.

There is additional support for low values of the common envelope efficiency from other systems studied in the literature. Reconstructing the evolution of post-common-envelope binaries of white dwarfs with main-sequence star companions, Zorotovic et al. (2010) found that most systems can be explained by a broad range of  $\alpha$  values, but they found simultaneous solutions for all post common envelope binaries in their sample only for  $\alpha = 0.2-0.3$  (also see Camacho et al. 2014). Toonen & Nelemans (2013) compared the synthetic and observed population of visible post common envelope binaries in the SDSS and also concluded that common envelope efficiency parameter must be low. Finally, Zorotovic & Schreiber (2022) reconstructed the evolutionary histories of post common envelope binaries with brown dwarf companions, and concluded that the vast majority of post common envelope binaries can be described with a small efficiency parameter.

Constraining the value of  $\alpha$  has significant implications for understanding the white dwarf merger rate and the outcome of the common envelope evolution. For example, Temmink et al. (2020) calculated an integrated merger rate (that leads to observable single white dwarfs) ranging from  $0.013$  to  $0.032 M_{\odot}^{-1}$ . The upper bound here is for a small common envelope efficiency parameter. The corresponding Galactic rate is  $0.04$  to  $0.09$  per year. The relatively high merger fraction that we found in our ultramassive white dwarf sample favors merger rates closer to the upper limit of this estimate.

## 6 CONCLUSIONS

We present the results from a comprehensive spectroscopic and photometric survey of the 25 ultramassive white dwarfs with  $M \approx$

<sup>2</sup> Even though the common envelope efficiency parameter  $\alpha$  is not well known, the structure parameter  $\lambda$  is constrained better (see the discussion in Toonen & Nelemans 2013). Hence, a small value of  $\alpha\lambda$  corresponds to a small value of  $\alpha$ , or an inefficient common envelope.

<sup>1</sup> These mergers contribute 45% of the systems in their default model.

$1.3 M_{\odot}$  identified by Kilic et al. (2021a). We use rapid rotation, kinematics, magnetism, and unusual atmospheric composition to identify merger candidates. We found 10 magnetic white dwarfs with field strengths ranging from a few MG to hundreds of MG, four of which have rotation periods in the minute to hour range. Four systems show large tangential velocities, and one object is a hot DQ white dwarf with a carbon dominated atmosphere. Several of our targets show multiple symptoms of being a merger product. J2211+1136 is the best example, it is ultramassive, highly magnetic, it rapidly rotates, and has a relatively large tangential velocity.

In total, we identify 14 objects out of 25 as likely merger systems, which implies a merger fraction of  $56^{+9}_{-10}\%$ . This fraction is higher than the predictions from the binary population synthesis calculations, but is closest to the models assuming a low common envelope efficiency parameter  $\alpha$ . Hence, our results provide further support to the low common envelope efficiency suggested by other authors studying post common envelope binaries of white dwarf plus main-sequence or brown dwarf companions.

Our follow-up photometric survey was designed to be inclusive of all targets, including normal DA stars, so that we do not miss any rapidly rotating systems. However, excluding the DA white dwarfs near the ZZ Ceti instability strip, we detected short period variability only among the magnetic white dwarfs in the sample. There is one more rapidly rotating system, J1832+0856 (Pshirkov et al. 2020), which is a DBA white dwarf. Hence, all of the rapidly rotating systems in our sample are either magnetic or non-DA white dwarfs. Phase-resolved spectroscopy of these rapidly rotating systems would be helpful for understanding the source of variability, whether it is due to a chemically inhomogeneous surface composition, rotational modulation of a complex magnetic field, and/or spots (e.g., Dupuis et al. 2000; Kilic et al. 2019; Caiazzo et al. 2021).

Even though our survey of 25 stars provides the first reliable observational constraints on the merger fraction of single ultramassive white dwarfs, a larger spectroscopic survey will be essential for increasing the sample size and extending the mass range probed. The Gaia EDR3 white dwarf catalog (Fusillo et al. 2021) includes 34 candidates with parallax  $\varpi \geq 10$  mas,  $M \geq 1.3 M_{\odot}$ , and  $T_{\text{eff}} \geq 8000$  K based on the pure hydrogen atmosphere model fits to the Gaia photometry and parallax. This number goes up to 324 candidates if we remove the parallax constraint. Follow up observations of such a sample can provide more precise estimates of the merger fraction of ultramassive white dwarfs.

Vera Rubin Observatory's Legacy Survey of Space and Time (LSST) will provide an unprecedented opportunity to identify the merger products among the solar neighborhood white dwarfs. The LSST will deliver  $\sim$ nightly cadence photometry for millions of white dwarfs and also parallaxes and proper motions for faint but nearby objects. Hence, the LSST will find both rapidly rotating white dwarfs and faint white dwarfs with large tangential velocities. The LSST, along with the upcoming large scale spectroscopic surveys like the Dark Energy Spectroscopic Instrument (DESI) Milky Way Survey (Allende Prieto et al. 2020) and the SDSS-V (Kollmeier et al. 2019), will significantly improve the merger fraction constraints, with implications for further constraining the physics of the common envelope evolution.

## ACKNOWLEDGEMENTS

This work is supported in part by the NSF under grants AST-1906379 and AST-2205736, the NASA under grant 80NSSC22K0479, the NSERC Canada, the Fund FRQ-NT (Québec), and by the Smith-

sonian Institution. AK acknowledges support from NASA through grant 80NSSC22K0338.

The Apache Point Observatory 3.5-meter telescope is owned and operated by the Astrophysical Research Consortium.

This paper includes data gathered with the 6.5 meter Magellan Telescopes located at Las Campanas Observatory, Chile.

Based on observations obtained at the international Gemini Observatory, a program of NSF's NOIRLab, which is managed by the Association of Universities for Research in Astronomy (AURA) under a cooperative agreement with the National Science Foundation on behalf of the Gemini Observatory partnership: the National Science Foundation (United States), National Research Council (Canada), Agencia Nacional de Investigación y Desarrollo (Chile), Ministerio de Ciencia, Tecnología e Innovación (Argentina), Ministério da Ciência, Tecnologia, Inovações e Comunicações (Brazil), and Korea Astronomy and Space Science Institute (Republic of Korea).

## DATA AVAILABILITY

The data underlying this article are available in the MWDD at <http://www.montrealwhitedwarfdatabase.org> and in the Gemini Observatory Archive at <https://archive.gemini.edu>, and can be accessed with the program numbers GN-2022A-Q-303, GS-2022A-Q-106, and GS-2022A-Q-303. The APO and McDonald Observatory data that support the findings of this study are available from the corresponding author upon reasonable request.

## REFERENCES

- Allende Prieto C., et al., 2020, *Research Notes of the American Astronomical Society*, 4, 188
- Bédard A., Bergeron P., Fontaine G., 2017, *ApJ*, 848, 11
- Bergeron P., Ruiz M.-T., Leggett S. K., 1992, *ApJ*, 400, 315
- Bergeron P., Dufour P., Fontaine G., Coutu S., Blouin S., Genest-Beaulieu C., Bédard A., Rolland B., 2019, *ApJ*, 876, 67
- Blouin S., Dufour P., Thibeault C., Allard N. F., 2019, *ApJ*, 878, 63
- Briggs G. P., Ferrario L., Tout C. A., Wickramasinghe D. T., Hurley J. R., 2015, *MNRAS*, 447, 1713
- Brinkworth C. S., Burleigh M. R., Lawrie K., Marsh T. R., Knigge C., 2013, *ApJ*, 773, 47
- Burgasser A. J., Kirkpatrick J. D., Reid I. N., Brown M. E., Miskey C. L., Gizis J. E., 2003, *ApJ*, 586, 512
- Caiazzo I., et al., 2021, *Nature*, 595, 39
- Camacho J., Torres S., García-Berro E., Zorotovic M., Schreiber M. R., Rebassa-Mansergas A., Nebot Gómez-Morán A., Gänsicke B. T., 2014, *A&A*, 566, A86
- Cheng S., Cummings J. D., Ménard B., Toonen S., 2020, *ApJ*, 891, 160
- De Rosa R. J., et al., 2014, *MNRAS*, 437, 1216
- Dufour P., Liebert J., Fontaine G., Behara N., 2007, *Nature*, 450, 522
- Dufour P., Fontaine G., Liebert J., Schmidt G. D., Behara N., 2008, *ApJ*, 683, 978
- Dufour P., Béland S., Fontaine G., Chayer P., Bergeron P., 2011, *ApJ*, 733, L19
- Dufour P., Blouin S., Coutu S., Fortin-Archambault M., Thibeault C., Bergeron P., Fontaine G., 2017, in Tremblay P. E., Gaensicke B., Marsh T., eds, *Astronomical Society of the Pacific Conference Series Vol. 509*, 20th European White Dwarf Workshop. p. 3 ([arXiv:1610.00986](https://arxiv.org/abs/1610.00986))
- Dunlap B. H., Clemens J. C., 2015, in Dufour P., Bergeron P., Fontaine G., eds, *Astronomical Society of the Pacific Conference Series Vol. 493*, 19th European Workshop on White Dwarfs. p. 547
- Dupuis J., Chayer P., Vennes S., Christian D. J., Kruk J. W., 2000, *ApJ*, 537, 977
- Ferrario L., Wickramasinghe D., Kawka A., 2020, *Advances in Space Research*, 66, 1025

- Fusillo N. P. G., et al., 2021, *MNRAS*,  
 García-Berro E., et al., 2012, *ApJ*, 749, 25  
 Genest-Beaulieu C., Bergeron P., 2019, *ApJ*, 882, 106  
 Hermes J. J., Kepler S. O., Castanheira B. G., Gianninas A., Winget D. E.,  
 Montgomery M. H., Brown W. R., Harrold S. T., 2013, *ApJ*, 771, L2  
 Hermes J. J., et al., 2017, *ApJ*, 841, L2  
 Holberg J. B., Oswalt T. D., Sion E. M., McCook G. P., 2016, *MNRAS*, 462,  
 2295  
 Hollands M. A., Tremblay P. E., Gänsicke B. T., Gentile-Fusillo N. P., Toonen  
 S., 2018, *MNRAS*, 480, 3942  
 Iben I. J., Tutukov A. V., 1984, *ApJS*, 54, 335  
 Isern J., García-Berro E., Külebi B., Lorén-Aguilar P., 2017, *ApJ*, 836, L28  
 Kanaan A., Kepler S. O., Giovannini O., Diaz M., 1992, *ApJ*, 390, L89  
 Kilic M., Rolland B., Bergeron P., Vanderbosch Z., Benni P., Garlitz J., 2019,  
*MNRAS*, 489, 3648  
 Kilic M., Bergeron P., Kosakowski A., Brown W. R., Agüeros M. A., Blouin  
 S., 2020, *ApJ*, 898, 84  
 Kilic M., Bergeron P., Blouin S., Bédard A., 2021a, *MNRAS*, 503, 5397  
 Kilic M., Kosakowski A., Moss A. G., Bergeron P., Conly A. A., 2021b, *ApJ*,  
 923, L6  
 Kollmeier J., et al., 2019, in Bulletin of the American Astronomical Society.  
 p. 274  
 Korol V., Hallakoun N., Toonen S., Karnesis N., 2022, *MNRAS*, 511, 5936  
 Maoz D., Hallakoun N., 2017, *MNRAS*, 467, 1414  
 Maoz D., Badenes C., Bickerton S. J., 2012, *ApJ*, 751, 143  
 Maoz D., Hallakoun N., Badenes C., 2018, *MNRAS*, 476, 2584  
 Moe M., Di Stefano R., 2017, *ApJS*, 230, 15  
 Montgomery M. H., Williams K. A., Winget D. E., Dufour P., DeGennaro S.,  
 Liebert J., 2008, *ApJ*, 678, L51  
 Mukadam A. S., Owen R., Mannery E., MacDonald N., Williams B., Stauffer  
 F., Miller C., 2011, *PASP*, 123, 1423  
 Nelemans G., Verbunt F., Yungelson L. R., Portegies Zwart S. F., 2000, *A&A*,  
 360, 1011  
 Pshirkov M. S., et al., 2020, *MNRAS*, 499, L21  
 Schimeczek C., Wunner G., 2014, *ApJS*, 212, 26  
 Schwab J., 2021, *ApJ*, 906, 53  
 Shen K. J., Kasen D., Miles B. J., Townsley D. M., 2018, *ApJ*, 854, 52  
 Temmink K. D., Toonen S., Zapartas E., Justham S., Gänsicke B. T., 2020,  
*A&A*, 636, A31  
 Toonen S., Nelemans G., 2013, *A&A*, 557, A87  
 Toonen S., Hollands M., Gänsicke B. T., Boekholt T., 2017, *A&A*, 602, A16  
 Tout C. A., Wickramasinghe D. T., Liebert J., Ferrario L., Pringle J. E., 2008,  
*MNRAS*, 387, 897  
 Tremblay P. E., Gianninas A., Kilic M., Ludwig H. G., Steffen M., Freytag  
 B., Hermes J. J., 2015, *ApJ*, 809, 148  
 Vanderbosch Z. P., Hermes J. J., Winget D. E., Montgomery M. H., Bell K. J.,  
 Nitta A., Kepler S. O., 2022, *ApJ*, 927, 158  
 Webbink R. F., 1984, *ApJ*, 277, 355  
 Williams K. A., Montgomery M. H., Winget D. E., Falcon R. E., Bierwagen  
 M., 2016, *ApJ*, 817, 27  
 Winget D. E., Robinson E. L., Nather R. D., Fontaine G., 1982, *ApJ*, 262,  
 L11  
 Zorotovic M., Schreiber M., 2022, *MNRAS*, 513, 3587  
 Zorotovic M., Schreiber M. R., Gänsicke B. T., Nebot Gómez-Morán A.,  
 2010, *A&A*, 520, A86  
 de Kool M., van den Heuvel E. P. J., Pylyser E., 1987, *A&A*, 183, 47

This paper has been typeset from a  $\text{\TeX}/\text{\LaTeX}$  file prepared by the author.